Research Square

Preprints are preliminary reports that have not undergone peer review.
They should not be considered conclusive, used to inform clinical practice,
or referenced by the media as validated information.

Fault Diagnosis for Satellite of Multi-Subsystems with Digital Twin Residual

Yu Shi
Beihang University
Xuelei Deng
CASIC Space Engineering Development Co., Ltd.
Yunfeng Dong
Beihang University
Fengrui Liu
frliu@buaa.edu.cn

Beihang University

Research Article

Keywords: Digital twin, Fault diagnosis, Satellite subsystem coupling, Model updating, Residual

Posted Date: July 15th, 2026

DOI: https://doi.org/10.21203/rs.3.rs-10340860/v1

License: This work is licensed under a Creative Commons Attribution 4.0 International License.
Read Full License

Additional Declarations: The authors declare no competing interests.

Fault Diagnosis for Satellite of Multi-Subsystems with Digital Twin Residual

Yu Shi[1]

School of Astronautics, Beihang University, Beijing 100191, China

Xuelei Deng[2]

CASIC Space Engineering Development Co., Ltd., Beijing 100039, China

Yunfeng Dong[3]

School of Astronautics, Beihang University, Beijing 100191, China

Fengrui Liu[4]

School of Astronautics, Beihang University, Beijing 100191, China

Abstract

Fault diagnosis for multi-subsystem satellites represents a critical technology for constructing resilient space architectures. However, current Digital Twin (DT)-driven fault diagnostic methods face several challenges, including limited modeling of subsystem couplings and difficulties in dealing with the complex characteristics of satellite fault data. To address these issues, this paper proposes a Digital Twin Residual (DTR)-driven fault diagnostic method for satellite of multi-subsystems. Coupling relationships between satellite subsystems are first incorporated into the modeling process. The satellite fault data are then analyzed and visualized, revealing the impact of residuals on diagnostic performance. Consequently, raw fault data are transformed into residual data, where fault-related features become more significant, enabling effective diagnosis. The proposed DTR method is validated on a satellite fault dataset containing 49 scenarios and achieves superior diagnostic performance against existing DT-driven fault diagnostic methods. This study offers a solution for DT-driven satellite fault diagnosis, contributing to increased reliability and resilience of space systems.

Key words: Digital twin, Fault diagnosis, Satellite subsystem coupling, Model updating, Residual

---

[1] Ph. D Student

[2] Associate Research Fellow

[3] Professor

[4] Professor, Corresponding author: frliu@buaa.edu.cn

1. Introduction

Fault diagnosis for satellite of multi-subsystems serves as a critical component in constructing resilient space architectures. As space increasingly becomes a focal strategic domain, ensuring space capabilities under adverse conditions, which is referred to as resilience [1], has become crucial. Satellites represent typical complex systems [2], composed of multiple subsystems, each comprising numerous components. Multi-subsystem satellite fault diagnostic methods identify faults based on sensor measurements acquired through telemetry. Intelligent fault diagnosis and recovery technologies enhance the satellite survivability in challenging environments, while a fundamental requirement of resilience is the provision of continuous service even under fault conditions [1]. Consequently, fault diagnosis for multi-subsystem satellites is a prerequisite for the establishment of resilient space architectures.

At present, the existing studies on satellite fault diagnosis mainly rely on feature processing approaches tailored to specific subsystems, while limited attention is given to comprehensive analysis across multiple subsystems. The Density Peak Clustering and Unsupervised Attribute Reduction (DPC-UAR) method identifies a minimal attribute subset from raw data to facilitate feature selection. This allows to perform automatic identification of clustering center, and to manage non-spherical data distributions, which increases the fault diagnosis accuracy for satellite power subsystems [3]. Chen et al. [4] proposed the Boruta Recursive Feature Elimination with Cross-Validation (BRFECV) algorithm, which allows to determine an optimal feature set, mitigating the impact of redundant features on diagnostic performance and achieving reliable fault diagnosis in the satellite Attitude and Orbit Control Subsystem (AOCS). Xia and Meng [5] developed base classifiers that extract downscaled fusion features using an enumerative approach, yielding a novel feature selection learning mechanism. This method enhances the AOCS fault diagnosis by identifying the most critical and relevant features within the classifier ensemble. Zhao et al. [6] first preprocessed raw data using Short-Time Fourier Transform (STFT) and Power Spectral Density (PSD) techniques, then proposed an Advanced Convolution Blocks-based CNN (ACBCNN) model to increase the feature extraction capability from PSD graphs, validating its effectiveness in AOCS fault diagnosis. It is important to note that the aforementioned studies focus on the fault characteristics of an individual subsystem. This reliance on feature extraction methods tailored to a specific subsystem makes the current studies on satellite fault diagnosis lack comprehensive analysis across multiple subsystems.

Deep neural networks (DNNs) can automatically extract features, which reduces the dependence on expert knowledge and enables fault diagnosis for multi-subsystem satellites. For instance, Han et al. [7] developed a fault diagnosis framework referred to as BLC-CNN, which integrates Convolutional Neural Networks (CNNs) for feature extraction, Bi-directional Long Short-Term Memory (Bi-LSTM) networks for feature denoising and fusion, and capsule networks for few-shot learning. This hybrid architecture significantly increases the processing capability for temporal data, allowing to perform direct fault classification from bearing vibration signals. Li et al. [8] proposed a framework based on CNN and Bi-LSTM, incorporating an attention mechanism allowing the deep network to focus on informative data segments, and facilitating the visualization of the learned diagnosis knowledge. Chen et al. [9] proposed a Deep Capsule Network adopting a Stochastic Delta Rule (DCN-SDR) technique that processes raw temporal signals as input and performs effective cross-domain fault identification. Leveraging their automatic feature recognition capability, DNNs directly use raw data as input for fault diagnosis, which enables fault diagnosis of multi-subsystem satellites.

DNN is a data-driven method [10, 11]. However, the satellite fault data measured by sensors are very limited, making data scarcity the main challenge faced in multi-subsystem satellite fault diagnosis. Data generation, such as physical experimentation [12] and modeling [13, 14], has been the main approach overcoming this limitation. Physical experimentation involves collecting fault measurement data from satellite subsystems in real space environments. However, because of the high production costs, the expenses of conducting satellite fault physical experiments are often prohibitive. Moreover, modeling methods face the challenge of developing satellite models that accurately represent coupling relationships between many subsystems. Multi-subsystem coupling refers to the relationships formed through the exchange and mutual influence of physical quantities among different subsystems. Such relationships cause a change in the state of one subsystem (especially under fault conditions) to directly or indirectly impact parameters of other subsystems. For instance, the AOCS and power subsystem are coupled, because the power generated by the solar panels is determined by the solar incidence angle, which depends on the attitude angle of the satellite controlled by the reaction wheels. In addition, reaction wheels adjust the attitude angle through rotational speed changes, which induce corresponding temperature variations caused by friction. Consequently, the AOCS is also coupled to the thermal control subsystem. The existing studies on satellite fault diagnosis mainly focus on modeling individual components or subsystems. Zhao et al. [6] proposed a modified particle swarm optimization-advanced convolution blocks-based CNN method to address the issues of overdesign and insufficient accuracy in CNN network design, achieving effective fault diagnosis for control moment gyroes. Mao et al. [15] developed a domain adversarial network-based method for fault diagnosis in satellite attitude control systems. Finally, Li et al. [16] established a satellite power system simulation platform and validated their proposed global sparse attention mechanism for diagnostic applications. They lack a comprehensive discussion on the critical relationship between real measurement data and satellite model parameters. As the performance parameters of actual satellites evolve over time, the diagnostic effectiveness of DNNs trained by satellite models may gradually deteriorate. As a result, a modeling method tailored to multi-subsystem satellites is crucial for effectively addressing data scarcity challenges.

The digital twin (DT) technology is an efficient data generation method in the field of fault diagnosis. Its core principles involve "a simulation system that integrates multidisciplinarity and multiphysics as well as the update of the virtual model using data from the physical entity" [2, 17]. Consequently, many studies explored the potential of DT-driven fault diagnosis approaches. For instance, Pengbo et al. [18] developed a DT model to simulate the dynamic and temperature rise characteristics of an induction motor in various fault scenarios, generating corresponding fault data as input to DNNs. Gong et al. [19] developed a DT for rolling bearings, which first transforms the fault data into the time-frequency domain through Short-Time Fourier Transform (STFT), then input them into a Vision Transformer-based network. The ability of DT to reveal the diagnostic process through explicit physical modeling and feedback mechanisms has been widely studied [20]. However, the existing DT-driven fault diagnostic methods still face several challenges when applied to satellites, which can be summarized as follows:

1. Multi-subsystem coupling is insufficiently considered in digital twin models that enable virtual-physical interaction. In satellites, subsystems exchange physical quantities and mutually affect each other, so a fault in one can directly or indirectly alter the parameters of others. However, existing DT-driven diagnostic methods have not adequately modeled these relationships. As a result, the simulation of fault propagation across subsystems is limited, hindering the further development of diagnostic methods towards multi-subsystem

scenarios.

2. Shortage of DT-driven fault diagnosis methods for handling complex features in satellite data. The existing methods typically train DNNs using raw fault data or data pre-processed with expert knowledge, such as STFT. However, these data comprise complex operational and fault characteristics, leading to performance bottlenecks for methods that optimize network architecture. Thus, a significant challenge consists in allowing DNNs to accurately identify fault features from the mixed characteristic present in satellite data.

To address the aforementioned challenges, this paper proposes the Digital Twin Residual (DTR) fault diagnostic method for satellite of multi-subsystems. Subsystems are first incorporated into a unified satellite model. A simulation framework, involving the coupling relationships based on calculating physical quantities between subsystems, is then established. Afterwards, the parameters of the model are updated using telemetry data from the Ladybird-1 satellite, which allows the DT model to accurately reflect the state of the satellite in the corresponding operational period. Based on fault occurrence probability and severity impact, 49 scenarios are designed to establish satellite fault dataset. Finally, a Temporal Convolutional Network (TCN) is trained. In the experimental validation, it is observed that training fails to adequately converge when using the raw fault state data as input. To study this limitation, a detailed analysis and feature visualization of the satellite fault data samples are conducted. A comparation between raw fault state, raw normal state, and residual data shows that residual processing reduces the complexity of satellite fault features and enables effective fault diagnosis of multi-subsystem satellite. The performance of DTR-TCN is validated through hyperparameter selection and comparative experiments. The main contributions of this paper are summarized as follows:

1. A methodological framework for constructing a digital twin model of multi-subsystem satellites is proposed. Through the exchange and mutual influence of physical quantities among subsystems, the modeling mechanism of coupling relationships is clarified. Moreover, the framework supports virtual-physical interaction. This framework enables the simulation of coupled parameter variations among different subsystems under various fault scenarios.
2. A DTR method for satellite fault diagnosis is proposed. By decoupling operational features from fault-related features in complex systems, the method enhances diagnostic capability. It is validated on a multi-subsystem satellite fault dataset containing 49 scenarios, and achieves outstanding diagnostic performance.

The remainder of this paper is organized as follows. Sect. 2 presents the digital twin modeling method. Sect. 3 details the proposed DTR method for multi-subsystem satellite fault diagnosis. Sect. 4 presents the results and discussion. Finally, the conclusion is drawn in Sect. 5.

2. Digital Twin Modeling Method

This paper proposes a DT modeling method for multi-subsystem satellite, allowing to address the challenges associated with modeling subsystem coupling relationships and establishing virtual-physical data interaction in satellites. A simulation framework is first developed based on the computational relationships between physical quantities across different subsystems, accurately reflecting the coupling relationships present in actual satellite systems. The virtual-physical interaction between satellite model parameters and telemetry data is then established using an NLS method. This allows the DT model to dynamically track and accurately mirror the varying state of the actual satellite over time, ensuring temporal synchronization between the DT model and its physical entity.

Satellites are complex systems comprising multiple subsystems, each exhibiting distinct coupling relationships with other ones. A typical satellite system consists of seven primary subsystems: Attitude and Orbit Control Subsystem (AOCS), power subsystem, thermal control subsystem, propulsion subsystem, Telemetry and Command Subsystem (TTC), structural subsystem, and payload subsystem. Multi subsystem coupling refers to the relationships formed through the exchange and mutual influence of physical quantities among different satellite subsystems. Such relationships cause a change in the state of one subsystem (especially under fault conditions) to directly or indirectly impact parameters of other subsystems. This multiphysics simulation process is a key factor of DT. The coupling relationships. The coupling relationships between these subsystems within the satellite model are illustrated in **Fig. 1**, where the circles denote individual subsystems while the directed lines between them, having the same color as the starting subsystem, indicate that the latter affects the ending subsystem.

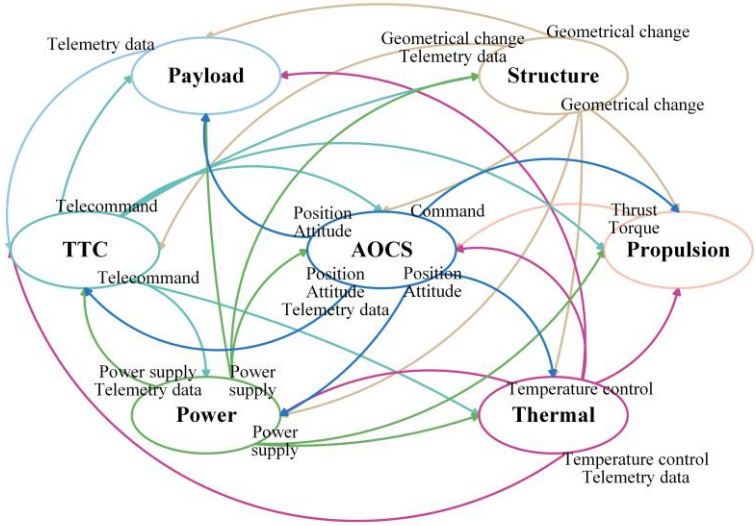

Fig. 1 Simulation framework of multi-subsystem satellite coupling relationships

The AOCS, power subsystem, and thermal control subsystem exhibit the strongest coupling relationships. They also have the highest failure probability and the most significant failure impact. The reaction wheel is a critical component within the AOCS that maintains strong coupling with other subsystems. Its main function consists in generating torque outputs for attitude control, which is expressed as:

$$M_{wheel} = M_m - M_{f0} - K_f \omega_{wheel}, \tag{1}$$

where M_m denotes the motor output torque, M_{f0} is the static friction torque of the bearings, K_f represents the friction coefficient, and ω_{wheel} is the rotation speed of the reaction wheel.

In torque mode operation, M_m is calculated as:

$$M_m = K_m V_i, \tag{2}$$

where K_m is the torque-voltage proportionality coefficient and V_i is the input voltage.

Therefore, the torque of the reaction wheel is affected by the voltage, which demonstrates the coupling relationship between the AOCS and the power subsystem.

K_f is calculated as:

$$K_f = \frac{\rho G C_{wheel} \Delta T_{wheel}}{0.1047 D_{bearing} \omega_{wheel}}, \tag{3}$$

where ρ and G are respectively the density and quantity of the lubricating oil, C_{wheel} is the specific heat capacity of the oil, ΔT_{wheel} denotes the temperature difference from the standard temperature of the reaction wheel, the constant 0.1047 represents the conversion factor from RPM to rad/s, and $D_{bearing}$ is the diameter of the bearings.

It can then be deduced that the temperature of the reaction wheel affects the flywheel torque, which reflects the coupling relationship between the AOCS and the thermal control subsystem.

The solar wing is one of the power subsystem components that accurately demonstrate the coupling relationship. It converts solar energy into electrical energy. Its electrical power output is computed as:

$$P_{wing} = C_{shadow} S_0 A_{wing} \eta X_{wing} \cos(\theta_{SW})(\beta_P \Delta T_{wing} + 1), \tag{4}$$

where C_{shadow} is a parameter used to identify whether the solar wings are in the shadow of Earth (also referred to as Earth shadow indicator), S_0 denotes the solar irradiance, A_{wing} represents the area of the photovoltaic array on the solar wings, η denotes the photoelectric conversion efficiency of the array, θ_{SW} is the angle between the normal vector of the solar wings and the direction of sunlight, β_P is the power temperature coefficient of the solar wings, X_{wing} is a set of additional coefficients, and ΔT_{wing} is the temperature difference from the standard temperature of the solar wings.

C_{shadow} is determined by the relative positional relationships between the Sun, Earth, and satellite, while θ_{SW} is calculated by the attitude relationship between the Sun and the solar wings. Consequently, P_{wing} is affected by both orbital and attitude. Eq. (4) indicates the variation of P_{wing} function of ΔT_{wing}, revealing the coupling relationship between the power and thermal control subsystems.

The thermal control subsystem is responsible for the thermal equilibrium management of the satellite system. The calculation of the temperature of the satellite is based on the nodes of the finite element model. The thermal equilibrium equation (in differential form) for a certain node of the satellite is given by:

$$\begin{aligned} T(t+\Delta t) = T(t) + \frac{\Delta t}{mc}(q_S(t) + q_E(t) + q_{ER}(t) \\ + q_{Rad}(t) + q_{Cond}(t) + P(t) - q_{OS}(t) - q_{IS}(t)) \end{aligned}, \tag{5}$$

where m and c respectively denote the mass and specific heat capacity of the node, $T(t)$ and $P(t)$ are the temperature and thermal power at time t, respectively. The various heat flux components include the solar radiation (q_S), Earth infrared radiation (q_E), Earth albedo radiation (q_{ER}), inter-nodal thermal radiation (q_{Rad}), inter-nodal thermal conduction (q_{Cond}), outer surface dissipation (q_{OS}), and internal surface dissipation (q_{IS}).

The thermal power $P(t)$ is the sum of thermal power from all the components within the node spatial domain, which can be expressed as:

$$P(t) = \sum_{k=1}^{N} C_{switch,k}(t) P_k(t), \tag{6}$$

where $C_{switch,k}$ and P_k represent the switching state and thermal power of component k, respectively.

For instance, the thermal power of an electrical heater is calculated as:

$$P_{heater} = I_{heater}^2 R_{heater} = \frac{U_{heater}^2}{R_{heater}}, \tag{7}$$

where I_{heater} denotes the current, U_{heater} represents the voltage, and R_{heater} is the resistance.

Therefore, Eqs. (4)-(7) present the coupling relationship between the thermal control subsystem and the power subsystem.

q_S at a specific node of the satellite is then determined as:

$$q_S = \alpha_s F_s \phi_{sr} A_{\text{node}}, \tag{8}$$

where α_s is the solar absorption coefficient of the exterior surface of the solar wings, F_s is the solar constant, ϕ_{sr} is the solar radiation angle, and A_{node} denotes the area of the node. Similar to the output power of solar wings, the solar radiation heat flux is also affected by the orbit and attitude.

Based on the aforementioned coupling relationships, a multiple subsystem satellite is modeled, while it still cannot accurately reflect the varying state of the actual satellite over specific time periods. Therefore, an NLS method is developed to update the parameters of the model, establishing virtual-physical interaction between simulation data and real telemetry data. This virtual-physical interaction represents the main difference between DT and traditional simulation method, enabling the model to reflect the state change of physical entity. The detailed workflow of the DT model updating is illustrated in **Fig. 2**. The first step consists in processing satellite telemetry data measured from physical entity. The telemetry data over specific time periods along with corresponding satellite parameter configurations are acquired. However, since these data are packaged according to the data transmission protocol, they cannot be directly aligned with simulation data for parameter updates. Therefore, the data packets undergo protocol parsing, followed by data cleaning and interpolation procedures for generating time-series data in a format compatible with that of the simulation data. The second step consists in generating data by the corresponding satellite model. During on-orbit operations, the parameters of the satellite will change due to many factors, such as aging and performance degradation in complex space environments. The initial parameters are measured before satellite launch, and thus using them to initialize the model will lead to gradually increasing error between simulation and telemetry data. The third step solves this problem by iteratively updating the parameters of the model, enabling virtual-physical interaction. The iterative process continues until the error converges, leading to optimized model parameters. Initiated by these parameters, the DT satellite model accurately reflects the operational state of the actual satellite in the specified time period.

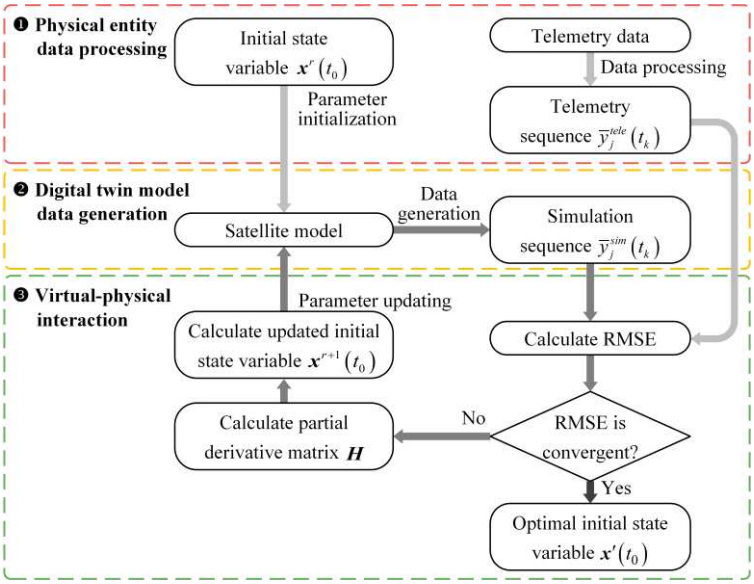

Fig. 2 Flow diagram of the DT model updating method

The value of the state variable at initial time t_0 for the r-th iteration is initially defined as $\boldsymbol{x}^r(t_0)$. Throughout the time interval $t \in [t_0, t_f]$, an error between the simulation sequence $\boldsymbol{y}^{sim}(t) = \left\{ \boldsymbol{y}^{sim}(t_k) \mid 0 \le k \le f \right\}$ and the telemetry sequence $\boldsymbol{y}^{tele}(t) = \left\{ \boldsymbol{y}^{tele}(t_k) \mid 0 \le k \le f \right\}$ from the actual satellite exists, which is represented by the Root-Mean-Square Error (RMSE). Therefore, a virtual-physical interaction between the actual satellite and the corresponding DT model is established to adjust the initial state variable $\boldsymbol{x}(t_0)$ and iteratively minimize the RMSE:

$$\min_{\boldsymbol{x}(t_0)} RMSE = \sqrt{\frac{\sum_{k=0}^{f} \left[\boldsymbol{y}^{sim}(t_k) - \boldsymbol{y}^{tele}(t_k) \right]^2}{f}} . \tag{9}$$

Satellites represent complex systems whose state variables dynamically vary over time. These state variables are measured by onboard sensors and then acquired by ground stations through telemetry, forming time-varying telemetry data streams. The relationship between the state variables x and telemetry variables y of the satellite can be expressed as:

$$\begin{cases} \dot{\boldsymbol{x}} = f(\boldsymbol{x}, t) \\ \boldsymbol{y} = h(\boldsymbol{x}, t) \\ x(t_0) = x_0 \end{cases}, \tag{10}$$

where f is the state equation, h is the observation equation, and x_0 is the initial value of the state variable. Due to the inherent nonlinearity in the state Eq. (10), mapping from the initial state to the simulation output is nonlinear. Therefore, minimizing the sum of squared residuals is an NLS problem.

Within the specified time range t, the m simulation and telemetry sequences are normalized as:

$$\bar{y}_j^{sim}(t_k) = \frac{y_j^{sim}(t_k) - y_{j,\min}}{y_{j,\max} - y_{j,\min}}, k = 0, \mathrm{L}\ , f, j = 1, \mathrm{L}\ , m, \tag{11}$$

$$\bar{y}_j^{tele}\left(t_k\right)=\frac{y_j^{tele}\left(t_k\right)-y_{j,\min}}{y_{j,\max}-y_{j,\min}},k=0,\mathrm{L}\ ,f,j=1,\mathrm{L}\ ,m, \tag{12}$$

where $y_{j,\min}$ and $y_{j,\max}$ are respectively the minimum and maximum values computed as:

$$y_{j,\min}=\min(y_j^{sim}(t_k),y_j^{tele}(t_k)),k=0,\mathrm{L}\ ,f, \tag{13}$$

$$y_{j,\max}=\max(y_j^{sim}(t_k),y_j^{tele}(t_k)),k=0,\mathrm{L}\ ,f\ . \tag{14}$$

Afterwards, the Newton-Raphson method is used to determine the least squares solution for the nonlinear model. The partial derivative matrix $\boldsymbol{H}$ of the normalized simulation sequence $\bar{\boldsymbol{y}}^{sim}$ with respect to $\boldsymbol{x}^r(t_0)$ at this point is expressed as:

$$\boldsymbol{H}=\left[\begin{matrix}\left[\frac{\partial\bar{y}_1^{sim}(t_0)}{\partial x_1^r}\mathrm{L}\ \frac{\partial\bar{y}_1^{sim}(t_f)}{\partial x_1^r}\right]^T & \mathrm{L} & \left[\frac{\partial\bar{y}_1^{sim}(t_0)}{\partial x_n^r}\mathrm{L}\ \frac{\partial\bar{y}_1^{sim}(t_f)}{\partial x_n^r}\right]^T\\ \mathrm{M} & \mathrm{O} & \mathrm{M}\\ \left[\frac{\partial\bar{y}_m^{sim}(t_0)}{\partial x_1^r}\mathrm{L}\ \frac{\partial\bar{y}_m^{sim}(t_f)}{\partial x_1^r}\right]^T & \mathrm{L} & \left[\frac{\partial\bar{y}_m^{sim}(t_0)}{\partial x_n^r}\mathrm{L}\ \frac{\partial\bar{y}_m^{sim}(t_f)}{\partial x_n^r}\right]^T\end{matrix}\right]_{\boldsymbol{x}^r(t_0)}. \tag{15}$$

The difference quotient, approximating $\boldsymbol{H}$ of the complex model, is computed as:

$$\frac{\partial\bar{\boldsymbol{y}}}{\partial x_i^r}\approx\lim_{\Delta x_i^r\to 0}\frac{\bar{h}_j\left(x_i^r+\Delta x_i\right)-\bar{h}_j\left(x_i\right)}{\Delta x_i},i=1,\mathrm{L}\ ,n,j=1,\mathrm{L}\ ,m, \tag{16}$$

where $\bar{h}$ represents the normalized observation equation.

The iterative update of $\boldsymbol{x}^r(t_0)$ using $\boldsymbol{H}$ is expressed as:

$$\boldsymbol{x}^{r+1}\left(t_0\right)=\boldsymbol{x}^r\left(t_0\right)+\left(\boldsymbol{H}^T\boldsymbol{H}\right)^{-1}\boldsymbol{H}^T\left(\bar{\boldsymbol{y}}^{tele}\left(t\right)-\bar{\boldsymbol{y}}^{sim}\left(t\right)\right). \tag{17}$$

The satellite model regenerates simulation data using the updated parameter $\boldsymbol{x}^{r+1}(t_0)$ as initial conditions. This iterative process continues until the RMSE converges, yielding the optimal initial values $\boldsymbol{x}'(t_0)$. When the satellite is aged or its performance is degraded, the model updating method ensures continuous synchronization between the DT model and the actual satellite. Therefore, the DT satellite model is developed with the virtual-physical interaction.

3. Proposed Fault Diagnostic Method for Satellite of Multi-Subsystems

3.1 Overall Framework

This paper proposes the Digital Twin Residuals (DTR) multi-subsystem satellite fault diagnosis framework illustrated in **Fig. 3**, allowing to address the limitations of the existing DT-driven fault diagnostic methods. The DT satellite modeling involves coupling relationships between subsystems. In addition, a model updating method enables effective interaction between virtual simulation data and physical measurement data. The DT model and the physical satellite exhibit consistent behavioral patterns at normal operating conditions, and therefore the processed residual data facilitates more effective identification of fault characteristics.

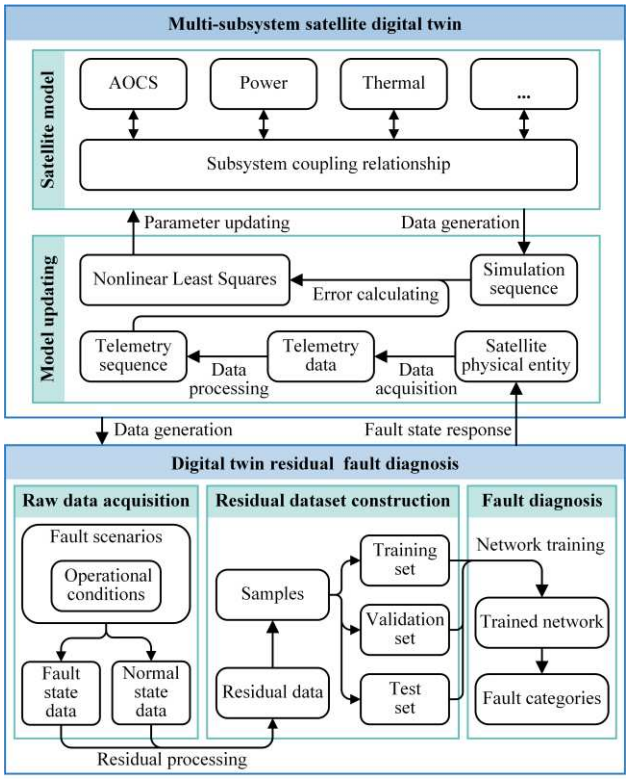

Fig. 3 Framework of the proposed multi-subsystem satellite fault diagnostic method

The proposed diagnostic framework comprises five key implementation steps as below:

1. Multi-Subsystem satellite modeling:

A multi-subsystem satellite model, incorporating subsystems (e.g., the AOCS, power and thermal control subsystems) and their intrinsic coupling relationships, is developed. This integrated model simulates the operational processes of the complete satellite, allowing to generate comprehensive simulation data.

2. DT model updating:

The parameters of the model are iteratively updated using telemetry data acquired from the actual satellite. This iterative process minimizes the error between simulation outputs $\boldsymbol{y}^{sim}$ and actual telemetry measurements $\boldsymbol{y}^{tele}$, establishing virtual-physical interaction between the DT model and its physical entity.

3. Raw data acquisition:

Fault scenarios across various subsystems and multiple satellite operational conditions are designed. The DT satellite model generates the data in normal $\boldsymbol{y}_{normal}$ and the data in fault states $\boldsymbol{y}_{fault,i}$, where *i* represents the fault category.

4. Residual dataset construction:

Data from normal and fault states are processed into residual data $\boldsymbol{y}_r = \boldsymbol{y}_{normal} - \boldsymbol{y}_{fault,i}$, which are then segmented into samples $s = \{y_r(t) \mid 0 \le t \le f\}$ of a specific length according to simulation operational conditions, and finally partitioned into training, validation, and test sets.

5. Fault diagnosis:

The DTR-TCN is trained by the constructed satellite fault dataset. During operational deployment, when faults occur in the actual satellite, the diagnostic system identifies their categories i by analyzing residuals between fault telemetry data and normal state simulation data. The diagnostic problem is thus formulated as a mapping process $s_i = y_r \rightarrow i$.

3.2 The DTR-TCN Fault Diagnostic Method

The proposed DTR fault diagnostic method addresses the limitations of the existing DT-driven fault diagnostic methods in handling complex characteristics within satellite fault data. Its workflow is illustrated in **Fig. 4**. The DT satellite model is employed to acquire fault and normal state data. Afterwards, residual processing is applied to the raw data in order to enhance fault-related features, leading to the construction of the satellite fault dataset. Finally, the DTR-TCN is trained to diagnose the fault of the multi-subsystem satellite.

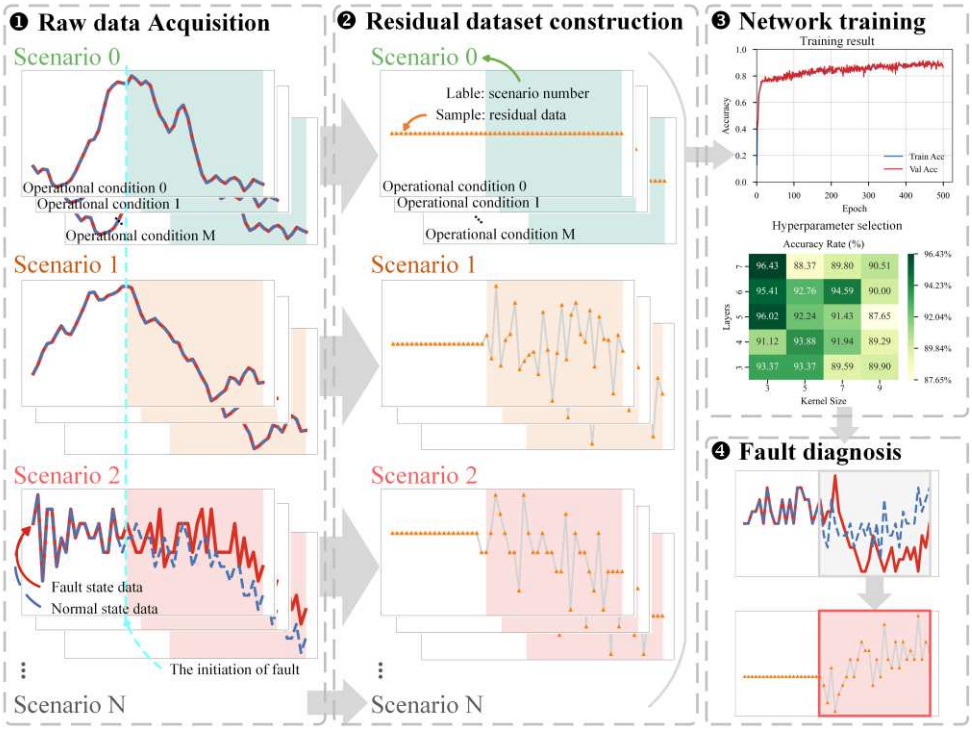

Fig. 4 Framework of proposed DTR fault diagnosis method

The DT satellite model serves as the foundation for generating raw data corresponding to various fault scenarios. Many fault scenarios, comprising different satellite subsystems, are designed. To enhance the dataset diversity, each scenario incorporates various operational conditions defined by distinct configuration parameters. For each operational condition, the model generates fault state data and corresponding normal state data. Fault information is injected at predetermined time during the simulation, triggering the DT satellite model to simulate the behavior at the specified fault scenarios. Consequently, after fault injection, the acquired raw data demonstrate distinct behavioral patterns between normal and fault states, effectively capturing the temporal evolution of fault across multiple subsystems.

The DTR fault diagnostic method is proposed based on the distinct behavioral patterns observed between the two data in fault scenarios. Fault state data exhibit complex characteristics comprising satellite operational and

fault characteristics. Operational characteristics are described as the normal behavioral patterns of the satellite, such as attitude maneuvers, battery charge/discharge management, and thermal balance control. In contrast, fault characteristics are described as the various fault patterns, such as constant bias, pulse errors, stuck faults, and open-circuit faults, which serve as key indicators for diagnostic method to identify fault types. Operational characteristics are present in normal and fault state data. This overlap reveals how fault characteristics can be more distinctly identified within residual data (i.e., the differential observations obtained when comparing normal state data with fault state data). Thus, in contrast to the existing methods employing raw fault state data, the use of residual data as input for diagnostic methods enables more effective processing of satellite fault features.

A satellite fault dataset is constructed to ensure that the diagnostic network is adequately trained. In this dataset, residual data serve as the samples, while the identifiers of their corresponding scenarios act as the labels. Each scenario comprises multiple sample-label pairs acquired from different operational conditions. All these pairs in different scenarios constitute the complete satellite fault dataset.

The TCN is efficient in processing time-series data due to its capacity to capture long-term dependencies, which is facilitated by an exponentially growing receptive field [21]. Accordingly, the proposed DTR-TCN uses residual data generated by a DT satellite model as its input to perform satellite fault diagnosis. The structure of the DTR-TCN is illustrated in **Fig. 5**. It comprises a convolutional layer, stacked TCN blocks, an adaptive max pooling layer, and a fully connected layer. For this multi-class classification task, the DTR-TCN is trained by minimizing a cross-entropy loss function. Its diagnostic performance is then evaluated using the metrics detailed in Sect. 2.

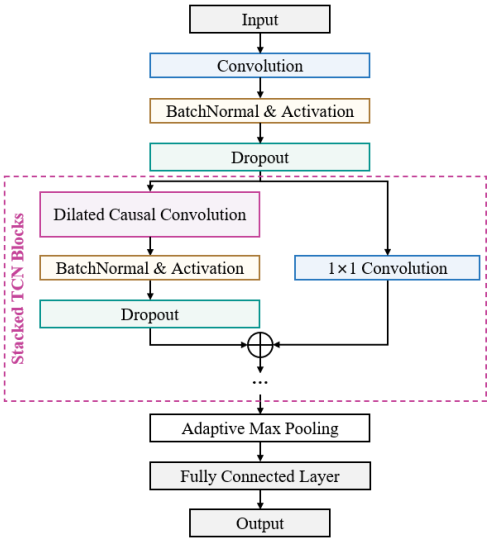

Fig. 5 Structure of the DTR-TCN

Finally, satellite faults are diagnosed using the DTR-TCN. At normal operational conditions, the DT satellite model acts as a companion model to the actual satellite. Telemetry data are continuously processed into residual data, used by the DTR-TCN to directly assess the current state of the satellite. Given the correspondence between the DT model and the actual satellite, the residual data under normal state remain almost invariant. On the contrary, the residual data under fault states exhibit more significant fault features. As a result, when a fault occurs, the DTR-TCN can accurately identify its features within the residual data to determine its specific type.

4. Results and Discussion

In this section, the Ladybird-1 satellite, launched on December 7, 2018, is used as a case study to evaluate the performance of the proposed DTR method in multi-subsystem satellite fault diagnosis. Based on the digital satellite development platform established in existing studies [22, 23] , a DT model of the Ladybird-1 satellite is developed. This platform enables rapid satellite model development through standardized configuration files that automatically generate C++ code frameworks for secondary development [24]. The parameters of the model are first updated using telemetry data from the Ladybird-1 satellite, where the convergence behavior of the error of the DT model is analyzed. Comparative data analysis demonstrates high consistency between the simulation outputs from the updated model and actual telemetry measurements. Comprehensive fault scenarios comprising multiple subsystems are then designed and a corresponding satellite fault dataset is constructed. The data samples vividly illustrate subsystem coupling relationships in fault conditions, while also highlighting the distinct characteristics between raw fault data and processed residual data. Finally, the impact of the residual processing on the diagnostic performance is further analyzed through feature visualization, and the performance of DTR-TCN in multi-subsystem satellite fault diagnosis is evaluated through hyperparameter selection and comparison experiments.

Modeling and diagnosis are performed using a Dell workstation equipped with Intel® Core™ i7-8700 CPU @ 3.20 GHz, 16 GB of RAM, and an NVIDIA GeForce GTX 1050 Ti GPU with 4 GB of VRAM. The software configurations of the modeling and diagnosis consist of C++ and Python, respectively.

4.1 Experimental Setup

4.1.1 Evaluation of the Multi-Subsystem Satellite Model

The parameters of the model are updated using on-orbit telemetry data from the Ladybird-1 satellite to minimize the RMSE. The convergence process of the RMSE throughout the iterative model update is illustrated in **Fig. 6**. The initial RMSE of 26.92% indicates that, although the DT model incorporates the subsystem coupling relationships of the actual satellite, the variation of the satellite parameters significantly affects the modeling error. Through iterative updates employing the NLS method, the RMSE converges to 9.42%, demonstrating a significant reduction in DT model error.

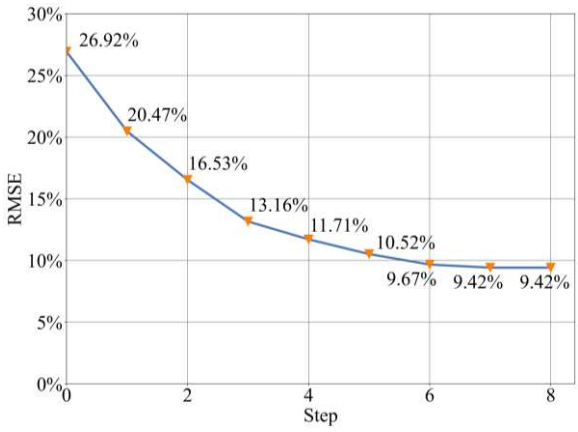

Fig. 6 RMSE convergence of the Ladybird-1 model using the proposed model updating method

Fig. 7 shows a comparison between telemetry data and simulation results from the Ladybird-1 model with residuals. Considering a sample of 1,000 s, the data in **Fig. 7** are segmented into nine groups comprising 22 variables. Each subplot contains an upper graph comparing telemetry data (solid lines) with simulation data (dashed lines), and a lower graph showing the corresponding residuals.

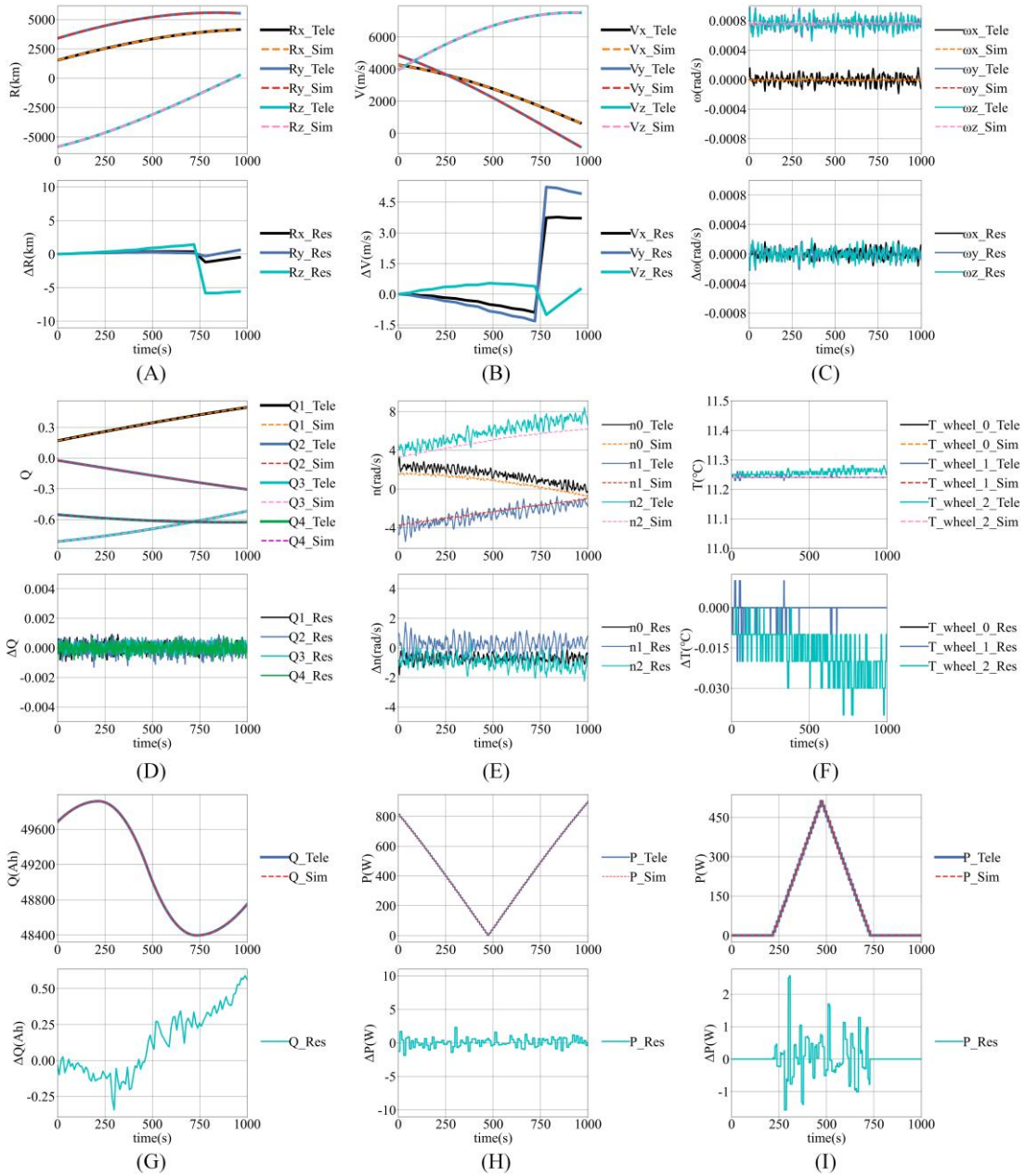

Fig. 7 Comparison between telemetry data and simulation results from the Ladybird-1 model with residuals: (A) Position, (B) velocity, (C) angular velocity, (D) attitude quaternion, (E) rotation speed of reaction wheel, (F) temperature of reaction wheel, (G) remaining capacity of battery, (H) output power of solar wing, and (I) discharge power of battery.

Figs. 7 (A/B) present the position and velocity of the satellite, respectively. The residual values are much smaller than the telemetry data, indicating high consistency between the simulated and actual satellite orbits. **Figs.**

7 (C/D) illustrate the variations of the angular velocity and attitude angle of the satellite, respectively. Minor fluctuations are observed in the telemetry data. They are attributable to disturbances in the attitude measurement and control processes. However, the simulation data closely approximate the telemetry data, demonstrating that the simulated attitude dynamics accurately represent the behavior of the actual satellite. **Figs. 7** (E/F) show the rotation speed and temperature variations of the reaction wheels, respectively. The former is correlated with the attitude variations, while the latter is affected by the variations of the rotation speed. Consequently, the attitude fluctuations trigger a chain reaction. Nevertheless, the simulation and telemetry data have consistent trends. **Figs. 7** (G)-(I) illustrate the parameter variations in the power subsystem. The output power of the solar wing depends on the incident angle of sunlight. The solar wing and batteries complementarily operate to maintain a stable power supply, exhibiting an inverse correlation. The changing state of the battery is jointly determined by the discharge power from the load and the charging power. In general, the simulation and telemetry data have consistent trends, and the residuals remain within a minimal range. These results demonstrate that the multi-subsystem satellite DT model leverages the proposed subsystem coupling modeling method and model updating to successfully simulate the coupling relationships between the subsystems and the temporal evolution of the physical entity.

4.1.2 Description of the Satellite Fault Dataset

In this section, the satellite fault dataset established through the multi-subsystem satellite DT model is detailed. The names and numbers of fault categories are presented in **Table 1**. Recent studies [25, 26] have demonstrated that these components show a high possibility of failure. The satellite fault dataset consists of 49 scenarios, including 48 fault scenarios and 1 normal scenario.

Table 1. Fault categories and numbers

Components	Fault Numbers	Fault Categories
Gyro	1-24	Stuck output; Saturated output; Gyro interference with constant bias or additional noise
Star sensor	25-36	Failed star sensor outputting a pulse, slope, constant gain, or constant stuck value; Star sensor interference with constant bias or additional noise
Reaction wheel	37-42	Idling reaction wheel; Stuck reaction wheel; Increasing friction
Solar wing	43-44	Solar wing angle reference loss; Erroneous solar wing rotation angle
Battery	45-48	Short circuit; Open circuit
Other	0	Normal state

More precisely, each scenario includes 90 telemetry variables, serving as the input of the diagnostic method. The detailed parameter names and identifiers are presented in **Table 2**. The gyroes, star sensors, and reaction wheels draw power from the batteries to determine and control the attitude of the satellite. Furthermore, the solar wings are responsible for charging the batteries. The flight mode of the satellite, recorded within the Center Manager Unit (CMU), highly depends on the variation of the attitude of the satellite, which serves as one of the key references for fault diagnosis.

Table 2. Telemetry variables and numbers

Components	Number	Telemetry Variables
Gyro	1-30	Angular velocity measurement; Voltage; Current; Electrical power; Operating status
Star sensor	31-52	Angular measurement; Voltage; Current; Electrical power; Operating status
Reaction wheel	53-68	Rotation speed; Expected acceleration; Torque; Voltage; Current; Electrical power; Operating status; Temperature
Solar wing	69-73	Output voltage; Output current; Output power; Deployment state; Operating status
Battery	74-89	Charging and discharging current/voltage/power; Charging indicator; Remaining capacity; Operating status
CMU	90	Flight mode

The data are collected in the model simulation process, with a sampling duration of 50 s at a rate of 1 Hz. Consequently, each sample contains 4,500 data points (90 parameters × 50 s). As the data are generated by a DT model, fault data can be cost-effectively obtained. To prevent data imbalance, the number of samples for each fault scenario is set equal to that of the normal scenario, with 100 samples per scenario. This yields 4,900 samples. The complete dataset is divided into training, validation, and test sets in a ratio of 6:2:2.

4.2 Experimental Results

4.2.1 Analysis of Residual Data

Fig. 8 shows a comparison between the raw fault-state data and the corresponding residual data for samples from the 9 fault scenarios presents in **Table 1**. The green vertical line, red solid line, and blue dashed line represent the initiation of fault at 20 s of the data sampling period, raw fault state data, and raw normal state data, respectively. The residuals between these two data are represented by orange markers.

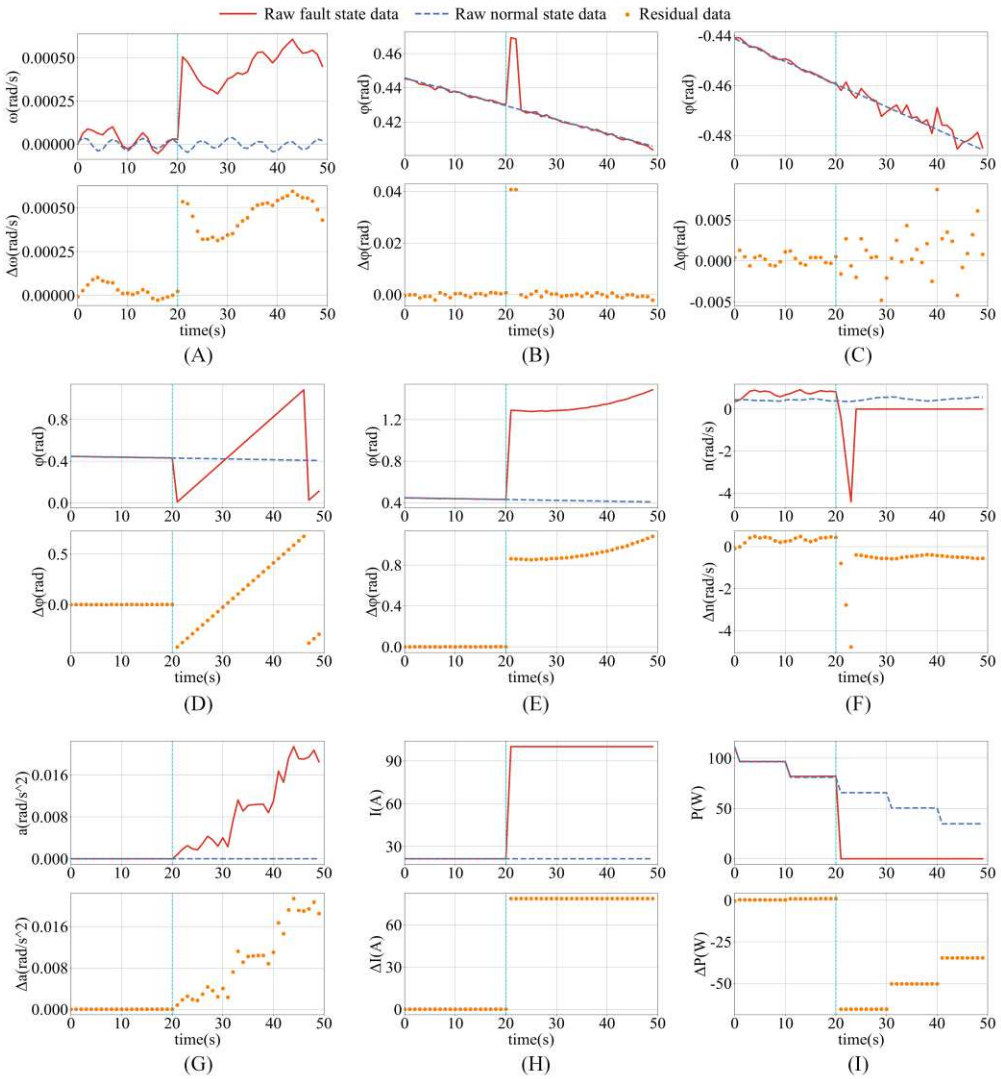

Fig. 8 Samples of fault scenarios: (A) Gyro with constant bias, (B) failed star sensor output a pulse value, (C) star sensor interference with additional noise, (D) failed star sensor output a slope value, (E) failed star sensor output a constant gain value, (F) reaction wheel stuck, (G) reaction wheel with increased friction, (H) discharge circuit short circuit, and (I) charge circuit open circuit.

More precisely, **Fig. 8** (A) illustrates the scenario of an increased constant bias in the gyro, where a constant error is added on its measurement. **Fig. 8** (B) shows the anomaly in the star sensor output, characterized by a pulse-type error added to the measured values. In **Fig. 8** (C), the random noise in the star sensor measurement significantly increases. **Fig. 8** (D) shows a case where the star sensor measurement changes to a slope-type output that does not correspond to the actual attitude variation. In **Fig. 8** (E), the star sensor measurement is amplified by a constant ratio. **Fig. 8** (F) presents the scenario of a stuck reaction wheel, where its rotational speed rapidly decreases and generates a pulse variation in acceleration. In **Fig. 8** (G), the friction torque of the reaction wheel increases, leading to more significant acceleration variations required to achieve the desired torque output. **Figs. 8** (H/I) represent a short circuit in the discharge circuit and an open circuit in the charging circuit, respectively. The former leads to a sharp current increase, while the latter makes the charging power decreases to zero. Residuals in all the subplots remain almost zero in normal conditions. In actual satellite applications, it is essential

to minimize the error between the satellite and its DT model. The fault features in the residuals vary in different fault scenarios, which is illustrated in the right of the green lines in **Fig. 8**. In addition, a comparison between the upper and lower subplots shows that fault features are more prominent in the residual data than in the raw fault state data in fault conditions. Consequently, in contrast to raw fault state data that feature a mix of signals, residual data with clear fault features provide a more robust basis for DTR-TCN.

Fig. 9 presents the variations of the six key variables from the stuck reaction wheel scenario (cf. **Fig. 8** (F)), further illustrating the subsystem coupling relationships under a fault scenario. The termination of the reaction wheel rotation deviates the attitude of the satellite from its nominal state, leading to increased residuals in star sensor measurements, as shown in **Fig. 9** (A). In addition, alterations in the solar altitude angle intensify the residuals in the output power of the solar wings (cf. **Fig. 9** (B)), which intensifies the residuals in the remaining battery capacity, as shown in **Fig. 9** (C). Moreover, the malfunctioning reaction wheel causes motor stalling and complete the termination of rotation, as shown in **Fig. 9** (D). This sudden variation provokes a pulse variation in acceleration (cf. **Fig. 9** (E)), leading to a temperature increase, as shown in **Fig. 9** (F). These variations demonstrate that, even under fault scenarios, the satellite DT model accurately reflects the coupling relationships between subsystems. The existing methods, which typically employ models of independent components, are often inadequate in capturing the impact of these coupling relationships in practical scenarios. However, a diagnostic method requires the incorporation of all the variables as inputs when diagnosing faults across various subsystems and components. Therefore, in real-world fault scenarios, ignoring these coupling relationships can significantly compromise the effectiveness of diagnostic method.

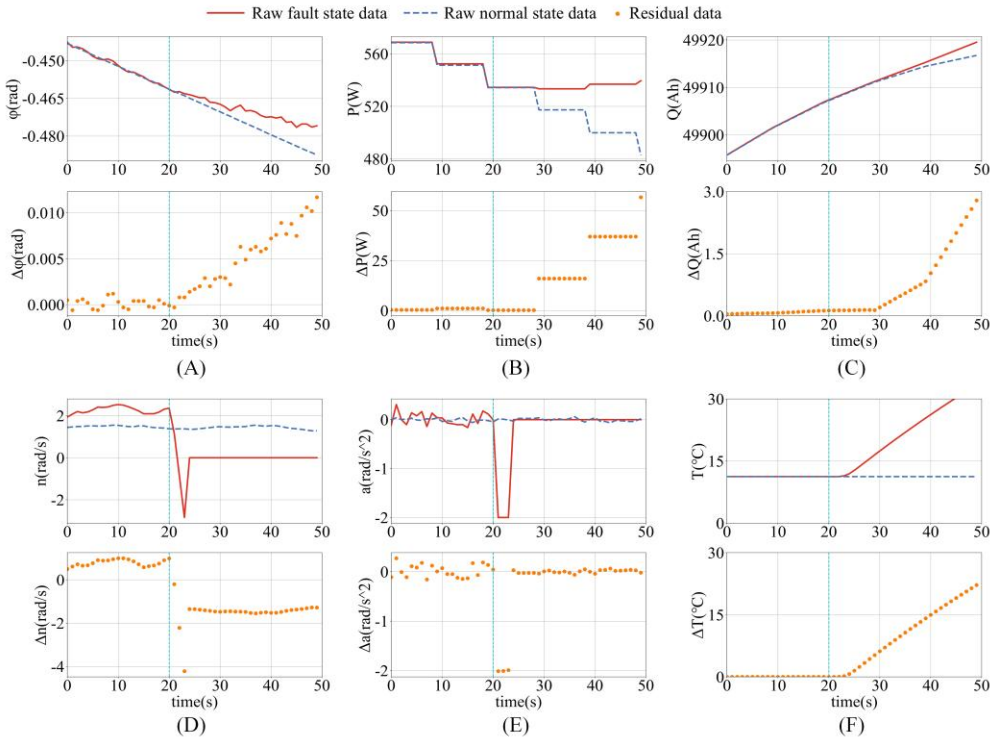

Fig. 9 Subsystem coupling relationships in a stuck reaction wheel scenario: (A) Star sensor measurements, (B) output power of solar wing, (C) remaining battery capacity, (D) rotation speed of reaction wheel, (E) acceleration of reaction wheel, and (F) temperature of reaction wheel.

4.2.2 Visualizing the Impact of Residual Data on Diagnostic Performance

In this section, the impacts of the residual and raw data on the diagnostic performance are analyzed. Although **Fig. 8** provides intuitive demonstration of the differences between raw fault state data and residual data, a further discussion is required to understand why these differences significantly affects the diagnostic performance. Thus, t-SNE visualization techniques are applied to raw fault state data and residual data at 49 fault scenarios in the satellite fault dataset. The obtained results are presented in **Fig. 10**. The raw fault state data in **Fig. 10** (A) exhibit a highly mixed distribution with low color discriminability, while the residual data in **Fig. 10** (B) demonstrate a clustering tendency with improved color discriminability. **Fig. 10** (B) shows that feature distributions corresponding to same fault scenarios maintain concentration, while distinct separation distances exist between feature clusters of different scenarios. This comparison demonstrates that residual processing significantly reduces the feature complexity of fault data.

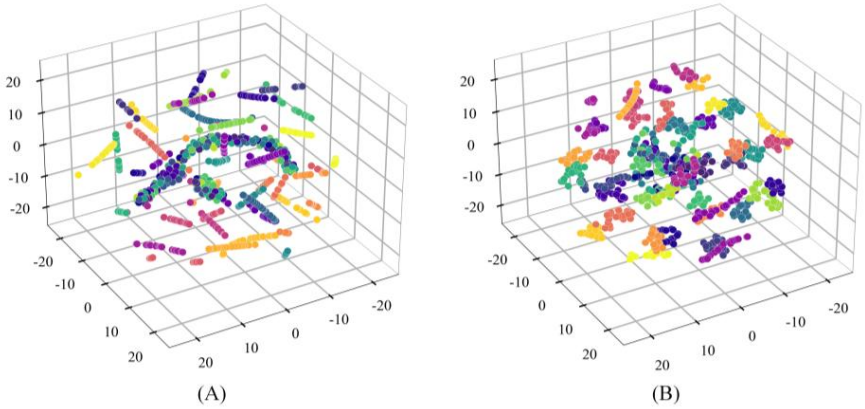

Fig. 10 Visualization of feature distribution: (A) Raw fault state data and (B) residual data.

To validate the impact of residual data on the diagnostic performance, the diagnostic network is trained separately using raw fault state data and residual data as inputs, and their diagnostic results are then analyzed. The visualization results of output features from the TCN blocks are presented in **Fig. 11**. The output features of the TCN blocks trained on raw fault data (cf. **Fig. 11** (A)) demonstrate limited cluster with significant feature overlap, indicating low discriminative capability for fault characteristics. On the contrary, the TCN blocks trained on residual data (cf. **Fig. 11** (B)) produce separated feature clusters with large inter-class distances, while features belonging to the same category form compact groupings. This comparative analysis further demonstrates that residual processing allows the diagnostic network to more effectively handle satellite fault data.

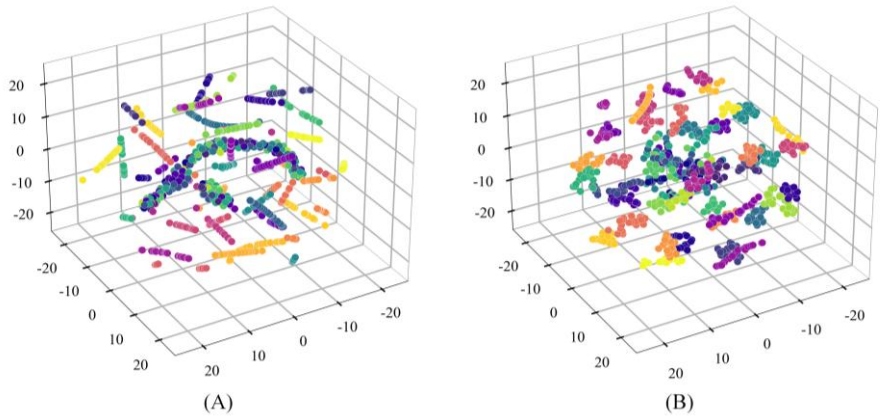

Fig. 11 Visualization of output features from the TCN blocks: (A) Trained on raw fault state data and (B) trained on residual data.

4.2.3 Hyperparameter Selection

To remove potential effects of hyperparameter selection on the diagnostic performance, a grid search method is employed for evaluating optimal hyperparameter combinations for the DTR-TCN. The number of TCN layers and convolutional kernel size are two key factors affecting the diagnostic accuracy. Given the input data length of 50 time steps, the hyperparameter value ranges are strategically determined to ensure sufficient receptive field coverage. Thus, layer numbers and convolution kernel sizes are explored within {3, 4, 5, 6, 7} and {3, 5, 7, 9}, respectively.

In this paper, the accuracy rate $r_{accuracy}$, F1-score, false alarm rate r_{FA}, and false negative rate r_{FN} are used to evaluate the performance of the satellite fault diagnosis algorithm. $r_{accuracy}$ is the ratio of accurately identified samples $N_{accuracy}$ to the total number of samples N_{total}:

$$r_{accuracy} = \frac{N_{accuracy}}{N_{total}} = \frac{\sum_{i=0}^{n}\sum_{j=1}^{m}\left|\left\{s_{i,j} \in S_i \mid D\left(s_{i,j}\right) = i\right\}\right|}{\left(n+1\right)\times m}. \tag{18}$$

The F1-score [27] is calculated as follows:

$$\mathrm{F1} = \frac{1}{n}\sum_{i=0}^{n}\left(2\times\frac{\mathrm{Precision}_i \times \mathrm{Recall}_i}{\mathrm{Precision}_i + \mathrm{Recall}_i}\right). \tag{19}$$

r_{FA} is the ratio of false alarms N_{FA} to the total number of samples identified as fault samples N_{IF}, representing the extent to which the diagnostic method erroneously issues fault alerts:

$$r_{FA} = \frac{N_{FA}}{N_{IF}} = \frac{\sum_{k=1}^{n}\sum_{j=1}^{m}\left|\left\{s_{0,j} \in S_0 \mid D\left(s_{0,j}\right) = k\right\}\right|}{\sum_{i=0}^{n}\sum_{k=1}^{n}\sum_{j=1}^{m}\left|\left\{s_{i,j} \in S_i \mid D\left(s_{i,j}\right) = k\right\}\right|}. \tag{20}$$

r_{FN} is the ratio of false negatives N_{FN} to the total number of actual fault samples N_{AF}, representing the extent to which the diagnostic method fails to respond under fault conditions:

$$r_{FN} = \frac{N_{FN}}{N_{AF}} = \frac{\sum_{k=1}^{n}\sum_{j=1}^{m}\left|\left\{s_{k,j} \in S_k \mid D\left(s_{k,j}\right) = 0\right\}\right|}{n \times m} \quad (21)$$

Fig. 12 shows the diagnostic performance of the DTR-TCN with different hyperparameter combinations on the satellite fault dataset. The metrics described in Section 2 are used to assess the optimal hyperparameter combinations. Note that superior metric values are indicated by darker color.

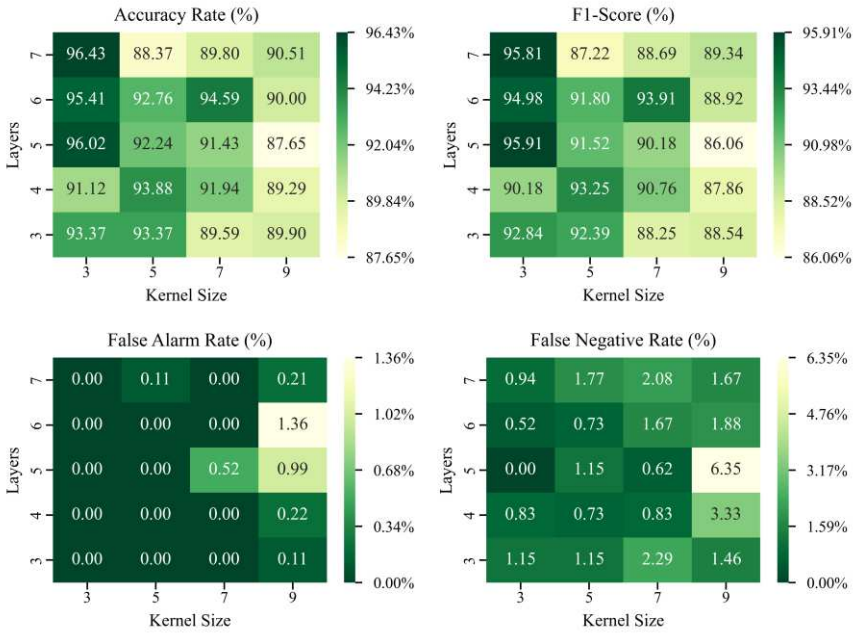

Fig. 12 Statistics of diagnostic results for different layers and kernel sizes.

It can be seen that, when the kernel size increases, the diagnostic performance is gradually decreased, which demonstrates that larger convolutional kernels reduce the sensitivity of the network to local features. The DTR-TCN achieves peak diagnostic accuracy greater than 95% (represented by the darkest regions in the heatmap) in the case of a kernel size of 3 and layer depths of 5, 6, and 7. Networks with fewer than 5 layers exhibit performance constraints due to insufficient receptive fields for capturing temporal dependencies. It can be clearly seen that the configuration with kernel size of 3 and 5 layers achieves optimal balanced performance, highlighted by zero false negative rate and false alarm rate.

4.2.4 Comparison Experiments

The diagnostic performance of the DTR-TCN is validated on the satellite fault dataset and compared with several existing methods, including network structures used in DT-driven diagnostic methods (CNN [28], DCBA [27], and DRSN [18]) as well as classical deep learning-based diagnostic methods (BLC-CNN [7] and LSTM [29]). The corresponding parameters and detailed network structures are presented below:

1. CNN [28]: The network comprises 3 convolutional layers and 2 pooling layers. The kernel size and number of filters are kept consistent with the original paper. In this study, the 2D convolutional layers are replaced with 1D layers to adapt to the 1D input data.
2. DCBA [27]: The network consists of a 1D-CNN, a BiLSTM, and an attention mechanism. The 1D-CNN

employs 64 filters with a kernel size of 3. The BiLSTM has 2 layers with 64 hidden units. The dimension of the attention mechanism is 128.

3. DRSN [18]: The network integrates a deep residual network, an attention mechanism, and a soft thresholding function. The deep residual network has 4 layers and a kernel size of 3.
4. BLC-CNN [7]: The network consists of a 2-layer CNN, followed by a bidirectional LSTM and a Capsule Network. The CNN employs 32 filters, the LSTM layer contains 64 hidden units, and the Capsule Network uses an 8-dimensional vector. Note that these parameters are all consistent with the original paper.
5. LSTM [29]: The network comprises 2 LSTM layers with 64 hidden units.

To mitigate overfitting, a dropout layer having a rate of 0.2 is incorporated into all the networks. During training, the Adam optimizer is employed for parameter updates, with an initial learning rate of 0.01. A cross-entropy loss is used. To ensure thorough convergence, the networks are trained for 500 epochs with a batch size of 512.

Fig. 13 shows a comparison between the diagnostic results. This evaluation uses 980 test samples, distributed across 49 scenarios as cataloged in **Table 1**, each comprising 20 test samples. Scenario 0 denotes the normal operational state, while the remaining ones denote various fault states. The diagnostic results are presented using bar charts, categorizing results into accurate diagnoses (green), false alarms (red), false negatives (orange), and other incorrect diagnoses (gray).

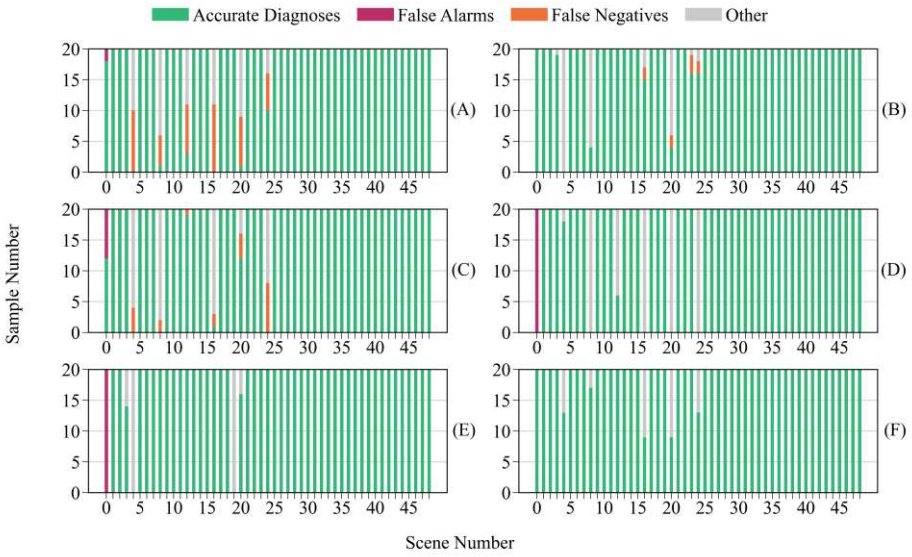

Fig. 13 Diagnostic results of CNN (A), DCBA (B), DRSN (C), BLC-CNN (D), LSTM (E), and DTR-TCN (F)

It can be observed that the DTR-TCN outperforms the other methods. The CNN, DCBA, and DRSN methods all exhibit false negatives, while false alarms occur in all methods except DCBA and the proposed DTR-TCN. Although BLC-CNN and LSTM achieve zero false negatives, some fault scenarios remain unrecognizable. In contrast, the proposed DTR-TCN achieves zero false alarms and zero false negatives. Moreover, despite some misclassifications among fault categories, there are no completely unrecognizable fault scenarios. Thus, the integration of the DTR method with the TCN enables optimal satellite fault diagnostic performance.

A statistical analysis of the diagnostic results is conducted to validate the performance and efficiency of the DTR-TCN. **Fig. 14** presents the statistics for all the test samples. It can be seen that the DTR-TCN achieves optimal values for the accuracy rate, false alarm rate, and false negative rate with the latter two reaching 0%. This demonstrates that, in practical applications, the diagnostic results obtained by the DTR-TCN have high reliability.

Given that satellite faults are rare events and the system nominally operates for most of its lifetime, the low rates of false alarm and false negative are critical. It eliminates the need for operators to expend extra effort for manually verifying the diagnostic results during long normal operations time, which is a decisive factor for the reliability of diagnostic systems in real-world deployment.

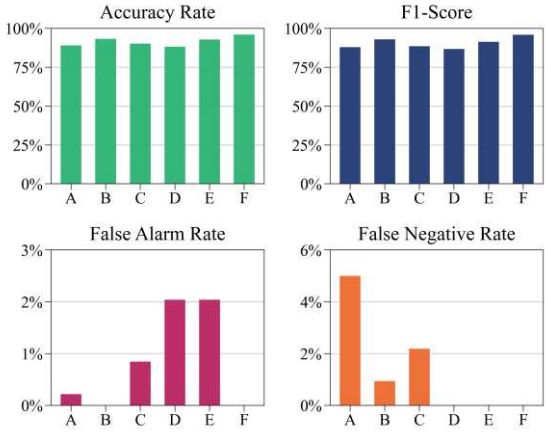

Fig. 14 Statistical diagnostic performance of the CNN (A), DCBA (B), DRSN (C), BLC-CNN (D), LSTM (E), and DTR-TCN (F)

Specific statistical results are presented in **Table 3**. The DTR method reduces the feature complexity of satellite fault data, allowing the CNN to achieve an accuracy of 89.08%. However, the limited capacity for processing sequential data of the CNN make it have a high false negative rate. On the contrary, the TCN leverages its architecture of dilated causal convolutions to effectively learn historical information from time-series data, consequently demonstrating optimal performance in satellite fault diagnosis. The accuracy and F1-score of the proposed DTR-TCN are improved by 2.95% and 3.21%, respectively, compared to DCBA. Moreover, the DTR-TCN accurately identifies normal scenarios, achieving false alarm and false negative rates of 0%. In summary, the DTR-TCN effectively addresses the challenge of processing complex features in multi-subsystem satellite fault diagnosis.

Table 3. Statistical diagnostic performance of the different methods

Diagnostic Method	Accuracy Rate	F1-Score	False Alarm Rate	False Negative Rate
CNN	89.08%	87.92%	0.22%	5.00%
DCBA	93.27%	92.93%	0.00%	0.94%
DRSN	90.20%	88.55%	0.84%	2.19%
BLC-CNN	88.16%	86.71%	2.04%	0.00%
LSTM	92.86%	91.41%	2.04%	0.00%
DTR-TCN	**96.02%**	**95.91%**	**0.00%**	**0.00%**

4.3 Analysis of Computational Efficiency

In aerospace engineering, the real-time performance of diagnostic methods directly impacts their practical applicability. Therefore, the computational efficiency of the diagnostic methods is analysed. **Table 4** summarizes the number of parameters, the average training time per epoch, and the average inference time per batch for each method. All methods are trained and tested on a unified hardware platform using the same dataset.

Table 4. Statistical computational efficiency of the different methods

Diagnostic Method	Parameters	Training time (s/epoch)	Inference time (ms/batch)
CNN	6641	2.05	0.22
DCBA	225906	2.14	0.56
DRSN	53021	6.87	0.45
BLC-CNN	435481	2.82	2.20
LSTM	80497	0.79	0.27
DTR-TCN	**61041**	**1.78**	**0.34**

The results show that the computational efficiency of the proposed DTR-TCN method meets the engineering requirements for real-time processing. Specifically, DTR-TCN contains only 61K parameters, which is significantly fewer than those of methods such as DCBA and BLC-CNN. Moreover, the average training time of DTR-TCN is 1.78 s per epoch, second only to LSTM, demonstrating high training efficiency. The average inference time of DTR-TCN is 0.34 ms per batch, outperforming most comparison methods and exhibiting strong real-time inference capability. In practical engineering applications, telemetry data are typically sampled at intervals of seconds or longer, whereas the inference time of DTR-TCN significantly shorter than the data acquisition cycle. Furthermore, the DTR-TCN processes 90 telemetry variables simultaneously, covering multiple subsystems within a single forward pass. Compared to diagnostic methods that use telemetry data from only a single component or subsystem as input, the DTR-TCN can diagnose multi-subsystem faults in a single process, thereby enhancing the overall computational efficiency of the diagnostic process. In summary, the computational efficiency of DTR-TCN satisfies the application demands of real-time diagnosis.

5. Conclusions

This paper proposes a DTR fault diagnostic method for multi-subsystem satellites, addressing limitations in the existing studies in terms of coupled modeling of satellite subsystems, virtual-physical interaction, and feature processing. A DT satellite model is developed by analyzing the relationships between physical parameters within subsystems. Model updates are performed using an NLS method, achieving interaction between the DT model and the actual satellite. As a result, the characteristics of residual data in fault scenarios are studied through sample analysis and feature visualization, leading to the proposed DTR-TCN. A case study, using the Ladybug-1 satellite as an example, is conducted to analyze the coupling relationships between subsystems and the consistency between simulation data from the DT model and telemetry data. The diagnostic performance of the DTR-TCN is validated on a satellite fault dataset comprising 49 scenarios. The results demonstrate that the residual data processing significantly reduces the complexity of fault features, allowing the TCN to more accurately identify faults. This study provides a reference for DT-driven satellite fault diagnosis studies.

For the future work, data-driven diagnostic methods for unknown faults or compound faults will be studied, along with other complex systems. In addition, cross-platform fault diagnostic methods applicable to different satellites will be investigated. In practical applications, future research on edge computing and intelligent maintenance systems will contribute to enhancing the reliability and resilience of future space systems.

Acknowledgements

This work was partially supported by the Key Laboratory of Spacecraft Design Optimization and Dynamic Simulation Technologies, Ministry of Education.

Data availability

The data that support the findings of this study are available from the corresponding author, upon reasonable request.

Declarations

The authors declare that they have no known competing financial interests or personal relationships that could have appeared to influence the work reported in this paper.

References

1. Lang K, Xu B, Simon M, Seibert B (2022) Automated Satellite Fault Detection using Machine Learning. In: ASCEND 2022. American Institute of Aeronautics and Astronautics, Las Vegas, Nevada & Online

2. Wright L, Davidson S (2024) Digital twins for metrology; metrology for digital twins. Meas Sci Technol 35:051001. https://doi.org/10.1088/1361-6501/ad2050

3. Suo M, Xing J, Ragulskis M, et al (2024) Fault diagnosis of satellite power system based on unsupervised knowledge acquisition and decision-making. Advanced Engineering Informatics 62:102768. https://doi.org/10.1016/j.aei.2024.102768

4. Chen S, Yang R, Zhong M, et al (2025) FWRF: Mitigating redundant features in fault diagnosis via feature weighted random forest. IEEE Trans Instrum Meas 74:1–11. https://doi.org/10.1109/TIM.2025.3550596

5. Xia H, Meng T (2025) A versatile feature selection learning method for satellite attitude control system fault diagnosis with limited data. Neurocomputing 619:129216. https://doi.org/10.1016/j.neucom.2024.129216

6. Zhao H, Liu M, Sun Y, et al (2024) Automated design of fault diagnosis CNN network for satellite attitude control systems. IEEE Trans Cybern 54:4028–4038. https://doi.org/10.1109/TCYB.2024.3384443

7. Han T, Ma R, Zheng J (2021) Combination bidirectional long short-term memory and capsule network for rotating machinery fault diagnosis. Measurement 176:109208. https://doi.org/10.1016/j.measurement.2021.109208

8. Li X, Zhang W, Ding Q (2019) Understanding and improving deep learning-based rolling bearing fault diagnosis with attention mechanism. Signal Processing 161:136–154. https://doi.org/10.1016/j.sigpro.2019.03.019

9. Chen T, Wang Z, Yang X, Jiang K (2019) A deep capsule neural network with stochastic delta rule for bearing fault diagnosis on raw vibration signals. Measurement 148:106857. https://doi.org/10.1016/j.measurement.2019.106857

10. Yang S, Wu J, Xie C, et al (2026) Data-Driven Intelligent Fault Diagnosis: A Review from the Perspectives of Three Practical Issues in Liquid Rocket Engines. Int J Aeronaut Space Sci. https://doi.org/10.1007/s42405-026-01131-9

11. Chen C, Zheng Q, Jiang F, Zhang H (2026) Fault Diagnosis for Aircraft Engines Based on Multi-task Graph SVM Inference with Individual Differences. Int J Aeronaut Space Sci 27:2294–2317. https://doi.org/10.1007/s42405-025-01062-x

12. Severson KA, Attia PM, Jin N, et al (2019) Data-driven prediction of battery cycle life before capacity

degradation. Nat Energy 4:383–391. https://doi.org/10.1038/s41560-019-0356-8

13. Saxena A, Goebel K, Simon D, Eklund N (2008) Damage propagation modeling for aircraft engine run-to-failure simulation. IEEE, Denver, CO, USA, pp 1–9

14. Sirajul Islam M, Rahimi A (2021) Fault Prognosis of Satellite Reaction Wheels Using A Two-Step LSTM Network. In: 2021 IEEE International Conference on Prognostics and Health Management. pp 1–7

15. Mao Z, Ma S, Liu W, Jiang B (2024) DCDAN-Based Incipient Fault Diagnosis for Satellite ACS Under Variable Operating Conditions. IEEE Trans Ind Inf 20:3115–3123. https://doi.org/10.1109/TII.2023.3299623

16. Li N, Xu Z, Wang P, et al (2026) Global sparse attention mechanism combined with transformer for fault diagnosis of satellite power system. Meas Sci Technol. https://doi.org/10.1088/1361-6501/ae26a0

17. Zhao W, Zhang C, Wang J, et al (2024) Application and research trend of digital twin in measurement technology. Meas Sci Technol 35:112003. https://doi.org/10.1088/1361-6501/ad6206

18. Pengbo Z, Renxiang C, Dong L, et al (2025) Digital twin-assisted fault diagnosis of induction motors with thermal analysis of inter-turn short circuit faults. Meas Sci Technol 36:066118. https://doi.org/10.1088/1361-6501/addbfe

19. Gong S, Li S, Zhang Y, et al (2024) Digital twin-assisted intelligent fault diagnosis for bearings. Meas Sci Technol 35:106128. https://doi.org/10.1088/1361-6501/ad5f4c

20. Zhao L, Xie T, Wei Y, et al (2025) Overview of digital twin-driven rotating machinery fault diagnosis: Status and trends. Meas Sci Technol 36:052001. https://doi.org/10.1088/1361-6501/adc8c3

21. Oord A van den, Dieleman S, Zen H, et al (2016) WaveNet: A Generative Model for Raw Audio

22. Dong Y, Li Z, Lei M (2021) Research on concept of digital satellite. Aerospace Shanghai 38:1–12. https://doi.org/10.19328/j.cnki.1006-1630.2021.01.001.

23. Min R, Yunfeng D, Chang L (2016) Code Generation Technology of Digital Satellite. In: Proceedings of ELM-2015 Volume 1. Springer, pp 511–519

24. Xie S, Li Z, Dong Y, Chen P (2024) Multigranularity Batch Sequential Design Method for Component-Level Satellite Design Optimization. IEEE Trans Aerosp Electron Syst 60:8779–8790. https://doi.org/10.1109/TAES.2024.3433325

25. Pourtakdoust SH, Fakhari Mehrjardi M, Hajkarim MH, Nasihati Gourabi F (2023) Advanced fault detection and diagnosis in spacecraft attitude control systems: Current state and challenges. Proceedings of the Institution of Mechanical Engineers 237:2679–2699. https://doi.org/10.1177/09544100231157132

26. Saleh JH, Castet J (2011) Spacecraft Reliability and Multi-State Failures: A Statistical Approach, 1st ed. Wiley

27. Hu X, Liu L, Quan Z, et al (2025) A novel integrated fault diagnosis method based on digital twins. Signals 6:18. https://doi.org/10.3390/signals6020018

28. Wu J, Shu Q, Li M, et al (2025) Research on deep learning rolling bearing fault diagnosis driven by high-fidelity digital twins. Int J Interact Des Manuf 19:1439–1450. https://doi.org/10.1007/s12008-024-01859-2

29. Belagoune S, Bali N, Bakdi A, et al (2021) Deep learning through LSTM classification and regression for transmission line fault detection, diagnosis and location in large-scale multi-machine power systems. Measurement 177:109330. https://doi.org/10.1016/j.measurement.2021.109330